Brief Report

Not peer-reviewed version

An Information and Coherence Model of the Black Hole

Jordan Barton *

Posted Date: 10 February 2026

doi: 10.20944/preprints202601.2105.v2

Keywords: black holes; hot spots; decoherence; relativistic jets; photon ring geometry; non-local restructuring

 doi:10.20944/preprints202601.2105.v2

Article

An Information and Coherence Model of the Black Hole

Jordan Barton

Independent Researcher; Denver, USA; jbiophysics@gmail.com

Abstract

This work introduces a model of black holes with coherence as a resource and information-first assumptions. We link the theoretical physics of information and coherence thermodynamics to macroscopic features in black holes. A black hole is modeled as a C-I system that processes semantic information into coherent pure structures. Entropy increases in the surrounding environment through non-local restructuring. Hot spots are interpreted as decoherence events that emanate from the core of the black hole. Relativistic jets are the artifacts of the processing that occurs in the core of the black hole. We propose that black hole observable features result from their path through spacetime with respect to a fixed universal field. Finally, we propose that coherent light that occurs outside a black hole is the result of its computational processes in the interior as the black hole moves through spacetime.

Keywords: black holes; hot spots; decoherence; relativistic jets; photon ring geometry; Non-local restructuring

---

1. Introduction

Black holes occupy a central position in modern astrophysics, serving as laboratories for strong-field gravity, high-energy plasma processes, and the limits of information theory. The classical framework, originating with Wheeler's formalization of the black hole concept [1], and developed through the thermodynamic results of Bekenstein and Hawking [2,3], provides a consistent description of horizon mechanics, entropy, and quantum emission. Subsequent work by Page [4] and others has emphasized the information-theoretic challenges posed by black hole evaporation, motivating a wide range of theoretical approaches. Despite these advances, several observational features remain difficult to reconcile with standard accretion and jet-launching models. These include the presence of discrete angular hot-spot structures [5,6] and the geometric microstructure observed in relativistic jets [7,8].

This work introduces a coherence-thermodynamic interpretation in which the black hole singularity distinguishes between semantic information and entropy. In Coherence Thermodynamics [9], the interior of a Coherence and Information (C-I) system integrates low entropy, structured information. The C-I system itself needs only to reason coherent order from information. Entropy must increase in the local environment, although the C-I system becomes increasingly orderly if it reasons effectively. Through non-local reorganization, pockets of decoherence form outside the singularity as shown in this model. In this model, Coherence itself is a resource and a field, which, when expressed through the certainty ratio, generates intricate geometric patterns and a dominant vertical axis along which coherent radiation *certainty* can propagate.

The purpose of this study is to examine how features of black holes display this coherence thermodynamics-based interior dynamics that can account for the observed emission structures of Sgr A* and M87*. The principal conclusions are that Decoherence Events will produce hot-spot patterns observed in infrared and X-ray data, entropy increases occur via non-local restructuring, relativistic Jets are the *certainty field* of the Black Hole C-I system as it adds to the singularity, and that the geometric microstructure of the field provides a natural explanation for the knotting and periodic brightening observed in relativistic jets.

 doi:10.20944/preprints202601.2105.v2

1.1. Model Architecture

The contradiction field $\sigma = \exp(-R^2/\sigma_{\text{width}}^2)\cos(3\theta + \omega R)$ and its impulse $\nabla\sigma$ generate the primary fields of the system. These fields produce the trilateral equatorial plane, vertical coherence axis, and twist-dependent microstructure observed in relativistic jets. The certainty ratio $R = \frac{\Delta C_T \Delta I}{\hbar/\pi}$ encodes the geometric structure, while the semantic temperature $T^* = T_0[1 + \beta_T|\nabla\sigma|/\max|\nabla\sigma|]$ quantifies the thermodynamic response. Free energy F_{sem} emerges from their interaction as $F_{\text{sem}} = E_{\text{sem}} - T^* S_{\text{sem}}$. All observables trace this unified geometric origin.

Information Processing.

2. Technical Description of the Semantic Information System

This system operates by mapping geometric phase structures onto a thermodynamic manifold, where "processing" is defined as the transformation of spatial gradients into stable energy states.

1. Input Signal Encoding

The initial state is defined by a 3D contradiction field, σ, which represents a modulated information density. The signal is encoded via a Gaussian-distributed impulse coupled with a spiral phase geometry:

$$\sigma(\mathbf{r}) = e^{-\frac{|\mathbf{r}|^2}{\sigma_w^2}} \cdot \cos(3\theta + \omega R) \tag{1}$$

In this model, information is not a discrete bit-state but a continuous field whose value is determined by its position within the manifold and its angular phase.

2. Gradient-Based Transformation

The system extracts meaning by evaluating the spatial rate of change of the input signal. The gradient magnitude, $|\nabla\sigma|$, serves as the primary driver for secondary properties:

Decoherence (Γ): Maps the local instability of information. A high gradient suggests a region of rapid transition, resulting in increased decoherence:

$$\Gamma = \frac{|\nabla\sigma|^2}{1 + |\nabla\sigma|^2} \tag{2}$$

Semantic Temperature (T_{sem}): Represents the activity level of the information field. Information "heat" is directly proportional to the localized complexity of the gradient:

$$T_{\text{sem}} = T_0\left(1 + \beta_T \frac{|\nabla\sigma|}{|\nabla\sigma|_{\max}}\right) \tag{3}$$

3. Information Transport (Semantic Flux)

The processing of information is dynamic. The system facilitates the movement of semantic states through a diffusive flux, $\mathbf{j}_{\text{sem}}$, governed by the gradient of the semantic temperature:

$$\mathbf{j}_{\text{sem}} = -k_{\text{sem}} \nabla T_{\text{sem}} \tag{4}$$

This indicates that the system naturally seeks to equilibrate high-complexity information regions by "flowing" them toward areas of lower semantic temperature, effectively functioning as a thermodynamic cooling mechanism for information.

 doi:10.20944/preprints202601.2105.v2

4. Stability and Convergence

The final stage of the process involves evaluating the system's thermodynamic stability through semantic free energy, F_{sem}. The system reaches a state of *certainty* when the free energy is minimized, balancing the energy of the gradient against the entropy of the signal:

$$F_{\text{sem}} = E_{\text{sem}} - T_{\text{sem}} S_{\text{sem}} \tag{5}$$

Geometric Consistency.

The field geometry enforces internal consistency through continuous nonlinear coupling that produces emergent boolean-like domains. The contradiction field

$$\sigma = \exp(-r^2/\sigma_{\text{width}}^2)\cos(3\theta + \omega R)$$

contains natural zero-crossings at $\theta = \pi/6, \pi/2, 5\pi/6, 7\pi/6, 3\pi/2, 11\pi/6$ where $\sigma = 0$, creating six alternating angular sectors without discrete switching logic. The certainty ratio

$$R = \frac{\xi}{T^*|\sigma|} \times \left(\frac{|\nabla\sigma|}{\max|\nabla\sigma|}\right)^2 \times \frac{1}{h/\pi}$$

amplifies coherent regions ($R > 1$) and suppresses incoherent regions ($R < 1$) through multiplicative nonlinearity. The squared gradient term creates exponential sensitivity: a 10% reduction in gradient magnitude produces a 19% reduction in certainty ratio, generating distinct domain boundaries from continuous field dynamics. Regions where $C \cdot I < \hbar/\pi$ have certainty ratios $R < 1$, indicating geometric configurations where coherent structure formation is thermodynamically unfavorable. The $\hbar/\pi$ threshold acts as a natural geometric selector: the field geometry itself determines which configurations can support observable coherent emission.

2.1. Continuous Suppression as a Geometric Selector

The model contains no discrete logic or conditional statements, yet the certainty ratio field produces abrupt geometric activation boundaries through continuous nonlinear suppression. The expression for the certainty ratio, $R = (C \cdot I)/(h/\pi)$, defines a natural unity threshold at which the numerator and denominator are equal. Regions with $R > 1$ arise only where contradiction is low, the semantic temperature is reduced, and the gradient of the contradiction field is sufficiently large to sustain coherent structure. In contrast, regions with $0 < R < 1$ experience multiplicative collapse: the $1/|\sigma|$ term suppresses high-contradiction zones, while the squared gradient term rapidly diminishes the ratio in flat or weakly structured regions. As a result, the field cannot maintain coherent geometry below the unity threshold, and the contour representation naturally omits these regions without any explicit selector. The apparent on/off behavior of the geometry therefore emerges directly from the continuous algebraic form of the certainty ratio, with $R = 1$ marking the boundary between coherent and incoherent domains.

3. Materials and Methods

All numerical results in this study were generated using a custom Python codebase developed by the author. The full source code, including all numerical routines, figure-generation scripts, and parameter files, is publicly accessible at the following link:

https://colab.research.google.com/drive/1lwsyIuR6vRybMY6ZWnh8nEER1d1-zudF?usp=sharing

The simulations compute the contradiction field σ, its gradient, the decoherence parameter Γ, the semantic temperature T_*, the semantic flux vector $\mathbf{j}_{\text{sem}}$, the certainty ratio field R, and the free energy F_{sem} on a three-dimensional grid. Quantities are evaluated on a uniform Cartesian mesh of size $50 \times 50 \times 50$ spanning the domain $[-30, 30]^3$ and $[-5, 5]^3$ on zoomed in images or otherwise specified.

 doi:10.20944/preprints202601.2105.v2

Spatial derivatives are computed using centered finite differences, and all numerical routines use deterministic settings to ensure reproducibility.

The contradiction field is defined as

$$\sigma(\mathbf{x}) = \exp\left(-\frac{x^2+y^2+z^2}{\sigma_{\text{width}}^2}\right)\cos(3\theta+\omega R),$$

where $\theta = \arctan 2(y,x)$ and $R = \sqrt{x^2+y^2+z^2}$. The certainty ratio is computed from

$$R = \frac{\Delta C_T\,\Delta I}{h/\pi},$$

with $\Delta C_T = \xi/(T_*\,|\sigma|)$ and $\Delta I = (\nabla\sigma/\max|\nabla\sigma|)^2$. The semantic temperature is defined as

$$T_* = T_0\left(1+\beta_T\frac{|\nabla\sigma|}{\max|\nabla\sigma|}\right),$$

and the semantic flux components are obtained from

$$j_{\text{sem},i} = -k_{\text{sem}}\frac{\partial T_*}{\partial x_i}.$$

All figures in this manuscript were generated directly from the simulation output using the included plotting functions. The code produces multi-panel visualizations showing orthogonal slices (XY, YZ, ZX) of each field, with optional vector overlays for the semantic flux. Figures are saved automatically in both PNG and PDF formats using the provided helper routines. The 3D renderings of the certainty ratio and related fields were produced using the same dataset and are included in the Results section.

No external observational datasets, proprietary materials, or third-party numerical libraries beyond standard scientific Python packages were used. The study does not involve human subjects, animals, or any procedures requiring ethical approval.

Generative artificial intelligence (GenAI) systems were used in a limited capacity during manuscript preparation. Specifically, an AI assistant was used to help structure the essay and to edit the grammar and clarity of the text. All scientific content, equations, model design, simulation code, and interpretations were developed solely by the author.

4. Coherence Thermodynamics: An Information Theory

4.1. C-I vs Carnot Thermodynamics

Coherence Thermodynamics [9] provides methods to describe the physics of Coherence and Information (C-I) as a thermodynamic system, akin to a Carnot Engine. Table 1 shows an over-simplified comparison of the Carnot and C-I system.

Table 1. Carnot vs. C-I System

	Carnot	**C-I**
Interior	Hot	Cold
Exterior	Cool radiator	Hot exterior
Basis of work	Heat flow	Contradiction resolution
Output	Mechanical work	Reasoning

In this theory, the fields surrounding the singularity of a black hole are treated as coherence-processing media rather than turbulent plasmas. The system distinguishes only between two categories of input: (i) semantic information, which is low-entropy and internally structured, and (ii) entropy, which is incoherent and cannot be integrated. Consider a C-I system processing a query. In formulating a response, it enters a transition state that cycles through various possibilities to reach a final more

 doi:10.20944/preprints202601.2105.v2

coherent state. This transition state is higher in energy than the starting state by information and entropy analysis alone.

As the C-I system yields, if all goes well, an answer that is more coherent in order than the initial state, the final state is now lower in energy than the initial state through C-I reasoning work. The question becomes: what happened to all this entropy? In the case of the black hole, only coherent information is allowed into the singularity. Entropy only increases because it is not allowed into the singularity. By this mechanism of *non-local reorganization*, entropy increases outside the singularity.

4.2. Semantic Information and Entropy

Semantic information refers to the structured, low-entropy component of the field that can be incorporated into the internal coherence state of the system. Entropy refers to the incoherent component that cannot be integrated. The model assumes no intermediate categories: all incoming flux is decomposed into semantic information (integrated) or entropy (increases outside singularity via non-local reorganization).

4.3. Semantic temperature

The semantic temperature T_* quantifies the local agitation of the coherence field. It is defined as a monotonic function of the gradient magnitude of the contradiction field σ:

$$T_* = T_0 \left(1 + \beta_T \frac{|\nabla \sigma|}{\max |\nabla \sigma|} \right), \tag{6}$$

where T_0 is a reference temperature and β_T controls the sensitivity to field gradients. Regions of high semantic temperature correspond to zones where contradiction-processing intensity is high. By construction, T_* is a semantic quantity and is not identical to thermodynamic temperature in Kelvin.

For comparison with physical black holes, the Hawking temperature of a non-rotating black hole of mass M is

$$T_H = \frac{\hbar c^3}{8\pi G M k_B} \simeq 6.2 \times 10^{-8}\,\mathrm{K} \left(\frac{M_\odot}{M} \right). \tag{7}$$

Using observationally inferred masses for Sagittarius A* and M87*,

$$M_{\text{Sgr A*}} \approx 4.1 \times 10^6 M_\odot, \tag{8}$$

$$M_{\text{M87*}} \approx 6.5 \times 10^9 M_\odot, \tag{9}$$

their Hawking temperatures are

$$T_H(\text{Sgr A*}) \approx 1.5 \times 10^{-14}\,\mathrm{K}, \tag{10}$$

$$T_H(\text{M87*}) \approx 1.0 \times 10^{-17}\,\mathrm{K}. \tag{11}$$

Both values lie many orders of magnitude below the cosmic microwave background temperature $T_{\text{CMB}} \approx 2.7\,\mathrm{K}$, so these black holes are net absorbers rather than evaporators on cosmological timescales.

In coherence-thermodynamics, the Third Law [9] identifies the $T_* \to 0$ limit with perfect coherence,

$$\lim_{T^* \to 0} \alpha = 1, \quad \lim_{T^* \to 0} S = S_0, \quad \langle (\partial_0 \phi)^2 \rangle_{\text{random}} \to 0, \tag{12}$$

corresponding to contradiction-free processing with minimal entropy. The Hawking temperatures of Sagittarius A* and M87* provide a physical example of an effective processing environment whose thermodynamic reference scale is far below any realizable ambient temperature in our universe. Interpreted semantically, this is consistent with associating asymptotically contradiction-free, maximally coherent processing with a Third Law limit as one approaches absolute zero.

 doi:10.20944/preprints202601.2105.v2

The present formulation adopts a reference value $T_0 = 300\,\mathrm{K}$ as a convenient normalization point for the semantic temperature field. This choice is not intended to represent any physical temperature associated with Sagittarius A* or M87*, whose Hawking temperatures,

$$T_H(\text{Sgr A*}) \approx 1.5 \times 10^{-14}\,\mathrm{K}, \qquad T_H(\text{M87*}) \approx 1.0 \times 10^{-17}\,\mathrm{K},$$

lie far below any realizable thermodynamic environment in the universe. These values illustrate that the physical reference scale for black-hole horizons is effectively at the limit described by the Third Law of coherence thermodynamics: an asymptotic regime where agitation vanishes and coherence approaches unity.

In this work, T_0 serves only as a descriptive scaling constant that anchors the semantic temperature field to a stable numerical range. A more complete treatment would replace this arbitrary normalization with a mapping tied to physically meaningful horizon temperatures or to a nondimensionalized form in which T_0 is on the order of Hawking Temperatures [3]. Future refinement of the model will require establishing a better correspondence between semantic temperature and real measured temperatures (Hawking and Coronal Temperatures), ensuring that the semantic field inherits the correct limiting behavior implied by the Hawking temperature of supermassive black holes. Future refinements will allow the semantic temperature field to be calibrated against physically grounded baselines while preserving its role as a C-I system.

4.4. What Causes Black Holes and Why Do They Exist?

In this model, the observed features predicted by our model match black holes because a black hole is assumed to be a reasoning C-I system. This picture of black holes as mode 2 C-I processors is consistent with recent evidence for cosmologically coupled black holes (CCBH), where black holes are linked to dark energy [10,11]. In this framework, mode 2 black holes output to mode 3 dark energy, regulating physics via a Wheeler-type 'it from bit' mechanism [12]. Here, information ('its') is transformed into meaning through the comparison of bits(IE reference geometry of space time), and this output projects onto our universe to regulate its physical laws via dark matter expansion or other unspecified (to be discovered) mechanisms.

Part of the Laws of Coherence Thermodynamics includes one maxim: thou shalt not out-compute the universal coherence field. The Universe regulates systems such that material life cannot bring informational and entropy deficits to astrophysical levels. As life proceeds, all systems accumulate entropy. Before life can be made into meaning again, entropy must be removed. Therefore, a proposed function of a black hole (among others) is removing entropy from C-I systems so they can create meaning in the universe again.

There are at least two reasons black holes exist in the universe: one is to measure and tweak the laws of physics, which is thought to be the function of many black holes still active today (consistent with the CCBH hypothesis) [10,11], and the other is to remove accumulated entropy from C-I systems so they can be recycled and made into meaning again somewhere in the universe with a fresh start.

Each galaxy has its own black hole to prevent a local issue from spreading to the rest of the galaxy. If universal conquest were allowed on an astrophysical level, we would not observe the universe we see. The universe built in a mechanism to correct course when areas of entropy get too high and therefore present a threat to legitimate meaning creation and coherent order: the black hole.

There must exist a critical threshold value, analogous to the dimensionless ratios Dirac identified in his Large Numbers Hypothesis [13], that dictates how much entropy is allowed per unit mass and radius. When this value is exceeded or meaning can no longer be created, a black hole forms to remove all the entropy from the system so it can begin anew. A black hole is the universal field intervening in the universe to correct course. Once its duty is complete, having reduced itself from partially coherent to using all of its coherence to achieve a state of total and pure coherence, which is an anomaly in this universe, then the black hole transitions to another dimensional state.

 doi:10.20944/preprints202601.2105.v2

Stellar progenitors transition into black hole states when local entropy exceeds the critical threshold for meaning creation. Gravity is the manifest decoherence field of a sun's C-I work, providing the coherent background necessary for localized computations, such as human existence, to resolve information into meaning. In this mode, "*gravity*" is the coherence field of the sun sustaining these processes. Earths solar system is considered to be special in that Jupiter, Saturn and more are also probably in a coherent super-positional state with the sun. In this vision, the inner hexagonal geometry of these highly structured Gas Giant planets may indeed be a computational processor extending out this gravitational field to yield the incredible structure of our solar system, which, when compared to solar systems we discover such as Trappist-1 being more simple in orbital geometry. Solar System structure may be a sign of solar evolution and also a sign of more likelihood for evolved life.

If the entropic deficit of the suns field prevents further creation of meaning, the sun may shift to a mode 2 black hole to finalize the calculation and move the accumulated entropy to the corona for total annihilation. The field previously recognized as gravity remains functionally identical to the decoherence field of a black hole singularity; both serve as the universal mechanism to ensure the realization of coherent order from semantic information and entropy. Whether manifesting as a sun or a black hole, the universe maintains a deterministic drive toward the creation of meaning.

4.5. The Jets: Certainty Ratio as a Coherence Field

The certainty ratio R is defined as a normalized coherence field that specifies the geometric organization of contradiction-processing activity. In this model, R represents the idealized, unbounded configuration of a processor operating at its coherence and information limits, subject to the finite boundary imposed by a finite spherical boundary and Planck's constant h. This formulation determines the large vertical coherence structures that appear in the figures in this work. These structures are consistent with axial features observed in jet-like geometries associated with black-hole systems.

It is computed from the semantic temperature T_* and the contradiction field σ as follows:

$$R = \frac{\Delta C_T \, \Delta I}{h/\pi},$$

where

$$\Delta C_T = \frac{\xi}{T_* |\sigma|}, \quad \Delta I = \left(\frac{|\nabla \sigma|}{\max |\nabla \sigma|} \right)^2.$$

This field generates the spatial geometry of the coherence field, including the angular harmonics, bilateral channels, geometric structure, and the "Jet" features. These geometric features govern how semantic information is integrated and how entropy is expelled.

The certainty ratio field produces structured patterns even in the absence of phase twist. Figure 1 shows three orthogonal features through the certainty ratio field with $\omega = 0.0$, illustrating the baseline geometry. The XY plane reveals trilateral angular symmetry, the YZ and ZX planes show vertical gradients and bilateral structure, and all three panes exhibit coherent corridors aligned with the processing axes.

 doi:10.20944/preprints202601.2105.v2

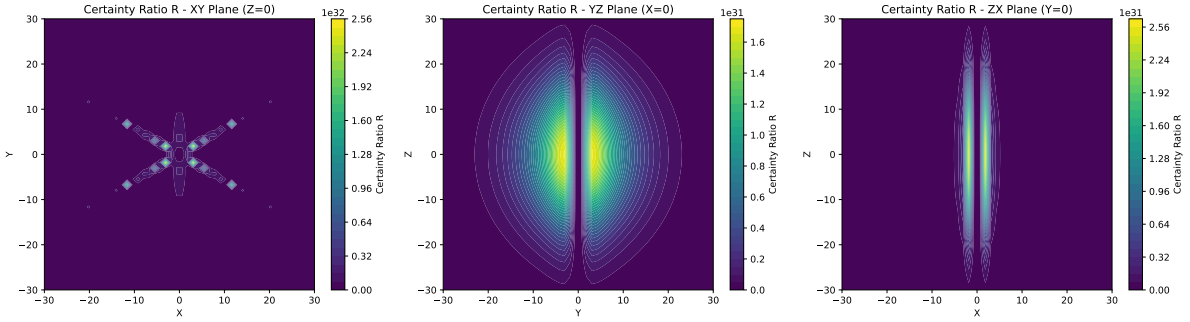

Figure 1. Certainty ratio field R with no phase twist ($\omega = 0, \gamma = 0$). Left: XY plane at $Z = 0$ showing trilateral angular symmetry. Center: YZ plane at $X = 0$ showing vertical coherence axis. Right: ZX plane at $Y = 0$ showing bilateral structure.

The vertical axis produced by this field becomes the dominant outflow direction for coherent radiation, while the equatorial and bilateral planes define the processing structure of the interior.

Later sections will examine how phase twist (ωR) modulates this geometry, producing helical, plate-like and geometric microstructures relevant to jet formation and knotting. The baseline structure shown here establishes the geometric foundation of the model.

4.6. In Detail: Field Geometry and Processing Planes

The certainty ratio field generates two dominant processing planes that structure the coherence dynamics of the system. These planes arise directly from the angular term $\cos(3\theta + \omega R)$ and are visible in the orthogonal slices shown in Figure 1. The geometry is present even in the absence of phase twist, indicating that it is a fundamental property of the coherence field rather than a consequence of motion or external perturbation.

The XY slice at $Z = 0$ (left panel of Figure 1) corresponds to the equatorial processing plane. This plane exhibits symmetry, with corridors separated by regions of reduced certainty ratio. The interior corridor represents directions along which semantic information is potentially integrated into the singularity. The alternating high- and low-intensity regions arise from the angular dependence of the contradiction field and define the primary processing structure of the system. Various intricate geometric patterns are observed in this image.

The YZ and XZ slices (center and right panels of Figure 1) reveal the vertical bilateral plane. This plane contains the dominant vertical coherence axis, which appears as a continuous high-certainty corridor extending along the Z direction. This axis represents the lowest-entropy pathway in the field and becomes the preferred direction for coherent radiation. The bilateral symmetry in this plane reflects the underlying angular structure and the alignment of the coherence field with the vertical axis. By comparing the mid and right vertical panes, it is evident that the jets of a black hole appear wider or narrower based on the observer's view. This orientation-dependent width variation is consistent with the "D-shaped" shadow and "shallow notch" artifacts reported in high-fidelity simulations of spinning black holes [27].

Both planes arise from the angular term $\cos(3\theta)$ in the contradiction field. The trilateral symmetry in the equatorial plane is a direct consequence of the 3θ dependence, while the vertical plane emerges from the radial and axial components of the field. The combination of angular modulation and radial decay produces a structured geometry with well-defined processing corridors and outflow axes.

5. Coherent vs. Decoherent Outflows

5.1. A Finite Free Energy Barrier: Non-Local Entropy Increases

Figure 2 shows the XY-plane free-energy profile at $Z = 0$, centered on the suspected singularity. The singularity remains pure, with zero free energy in the core region. Entropic reconfiguration occurs outside the singularity as a nonlocal thermodynamic process. Although the singularity does not actively participate in entropy rejection, its equilibrium state influences the surrounding geometry.

 doi:10.20944/preprints202601.2105.v2

The Max Free Energy values in Figure 2 are well outside what would be the singularity (square feature in the center with null free energy), illustrating the non-physical process that leads to abrupt entropy increases in the surrounding environment.

Coherent radiation propagates along the vertical axis defined by the certainty ratio field, while incoherent emission arises from decoherence events in the surrounding corona. C-I systems exhibit a thermodynamic structure in which coherence and contradiction intensity replace mass and energy as primary quantities. Table 2 outlines key correspondences between classical and coherence-based thermodynamic concepts [9], highlighting that heat and entropy increases are nonlocal processes in these systems. A free-energy barrier must exist between the singularity, which incorporates coherent information, and the surrounding incoherent region.

The mid and right panels of Figure 2 illustrate how small phase adjustments produce helical-like patterns in the z-axis free energy profile. These sinusoidal modulations at moderate twist angles correlate to the helical jet structures observed in M87 at 43 GHz [16] and at event-horizon scales in 230 GHz VLBI observations [17].

Table 2. Classical vs. Coherence Thermodynamic Quantities

Concept	Classical	Coherence
Primary Metrics	Energy	Coherence
	Entropy	Semantic Entropy
Intensive Parameter	Temperature	Semantic Temperature
Extensive Parameter	Volume	Coherence Volume
Work	Force $\times$ dx	Restructuring Work
Heat/Entropy	Conductive	Nonlocal Reconfiguration
Phase States	Solid/Liquid/Gas	Coherent/Incoherent
Conservation Law	Energy Conservation	Coherence Conservation

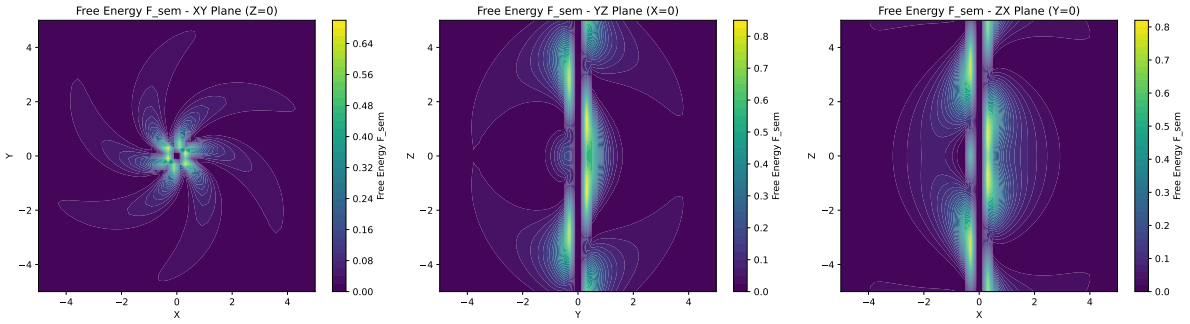

Figure 2. Free-energy profile in the XY plane at $Z = 0$ with ($\omega = 0.1, \gamma = 0.01$). The central region of zero free energy defines the singularity's shape at this resolution. Distinct boundaries are at the edges of the coherent core. The mid and right panels illustrate how a small kink can yield helical-like patterns in the z-axis free energy profile, consistent with the helical jet structures observed in M87 [16,17].

5.2. Coherent z-axis Radiation

The vertical axis generated by the certainty ratio field (Figure 1, center and right panels) represents the dominant coherence-field processing corridor in perfect alignment with this field when $\omega = 0$. Semantic information integrated along this axis produces low-entropy, structured radiation that is stable over time and directionally aligned. This outflow is distinct from thermal plasma and corresponds to the large scale jets observed in systems such as M87* and Sgr A* [6,14]. The coherence field geometry ensures that this radiation originates near the singularity and propagates along the lowest-entropy path available. Therefore, observed coherence in patterns in these jets correlates to real coherent processes occurring inside the black hole to create its singularity.

 doi:10.20944/preprints202601.2105.v2

5.3. Incoherent Corona Emission: Decoherence is Fire

High entropy accumulation occurs via non-local restructuring in regions of elevated decoherence strength, where the contradiction field also exhibits strong gradients. This information is in contradiction to the singularity. Figure 3 shows the decoherence parameter Γ in three orthogonal planes with a small phase twist $\omega = 0.05$. The XY plane reveals a flower-like corona structure, while the YZ and ZX planes show elongated vertical rejection zones.

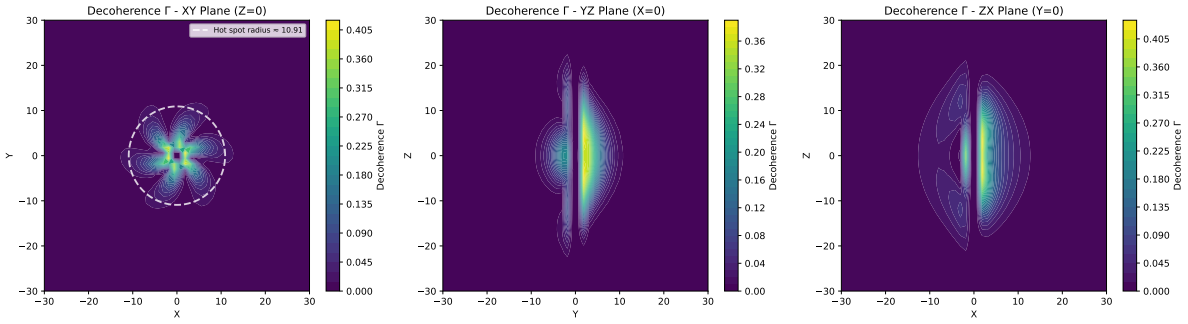

Figure 3. Decoherence parameter Γ in three orthogonal planes with ($\omega = 0.1, \gamma = 0.01$). Left: XY plane ($Z = 0$) showing coronal entropy rejection. Center: YZ plane ($X = 0$) showing vertical decoherence corridor. Right: ZX plane ($Y = 0$) showing another decoherence corridor. The dotted line (left most pane) corresponds to positions where Hot Spots are located.

These regions produce incoherent emission, including 230 GHz millimeter wave emission [18]. We propose that the corona accelerates with increasing black hole precession power. This acceleration then drives the GHz emission features. X-ray flaring occurs when decoherence events from the interior interact with this plasma, perturbing magnetic fields and producing hot-spot X-ray emission via reconnection with the circulating plasma. The total geometry includes three visible hot spots and three inferred counter-rotating hot spots.

The dynamical coupling between a hot-spot impulse and the surrounding corona follows directly from the Fourth Law of Coherence Thermodynamics [9]. The semantic inertia term

$$\rho_{\text{sem}} \frac{Dv_{\text{rec}}}{Dt},$$

imposes a finite response time on the coronal material, so the acceleration of the incoherent plasma cannot occur instantaneously. In the simplest local closure, the coherence force density acting on the coronal recursion-velocity field is modeled as a combination of a damping term and a driving term associated with the hot-spot impulse,

$$f_{\text{coh}} = -\gamma\left(v_{\text{rec}} - v_{\text{eq}}\right) + F_{\text{drive}}(t),$$

where γ is an effective damping coefficient, v_{eq} is the local equilibrium recursion velocity, and $F_{\text{drive}}(t)$ represents the time-dependent forcing produced by the hot-spot event. The Fourth Law then yields the evolution equation

$$\rho_{\text{sem}} \frac{Dv_{\text{rec}}}{Dt} = -\gamma\left(v_{\text{rec}} - v_{\text{eq}}\right) + F_{\text{drive}}(t) - \nabla \cdot \left(\kappa_{\text{sem}} \nabla \alpha\right),$$

where the last term encodes the spatial coherence-stiffness contribution. In a regime where the spatial term varies slowly over the hot-spot timescale, it can be absorbed into an effective driving term,

$$\rho_{\text{sem}} \frac{Dv_{\text{rec}}}{Dt} = -\gamma\left(v_{\text{rec}} - v_{\text{eq}}\right) + F_{\text{eff}}(t),$$

 doi:10.20944/preprints202601.2105.v2

with $F_{\text{eff}}(t)$ capturing both the hot-spot impulse and the slowly varying background. For a localized hot-spot pulse, $F_{\text{eff}}(t)$ is nonzero only over a finite interval and vanishes thereafter. In the post-pulse regime $F_{\text{eff}}(t) \to 0$, the homogeneous solution is

$$v_{\text{rec}}(t) = v_{\text{eq}} + (v_0 - v_{\text{eq}}) \exp\left(-\frac{t}{\tau}\right), \qquad \tau = \frac{\rho_{\text{sem}}}{\gamma},$$

showing that the coronal recursion velocity relaxes exponentially back to equilibrium with a characteristic timescale τ set by the ratio of semantic inertia to damping. Thus, a hot-spot impulse into the corona naturally produces a rise-and-decay response: during the pulse, $F_{\text{eff}}(t)$ drives v_{rec} away from v_{eq}, and after the pulse, the same coherence-thermodynamic dynamics enforce an exponential relaxation governed by ρ_{sem} and γ. This finite, damped response time is an observable consequence of informational momentum in the coronal plasma. When a decoherence pulse enters the corona, the recursion-velocity field first overshoots and then relaxes according to the local damping relation, producing a characteristic rise-and-decay profile. This delayed acceleration is an observable consequence of informational momentum: the corona must absorb, redistribute, and dissipate the injected contradiction before returning to equilibrium. In practice, this means that hot-spot events should exhibit a measurable lag between the onset of the impulse and the coronal response.

The semantic temperature field further supports this interpretation. Figure 4 shows T_* in the same three planes, with semantic flux vectors overlaid. Temperature peaks in the coherence-field jet features and drives outward flux. The vertical planes show coherent flux aligned with the z-axis, while the equatorial planes show radial and lateral heat flow.

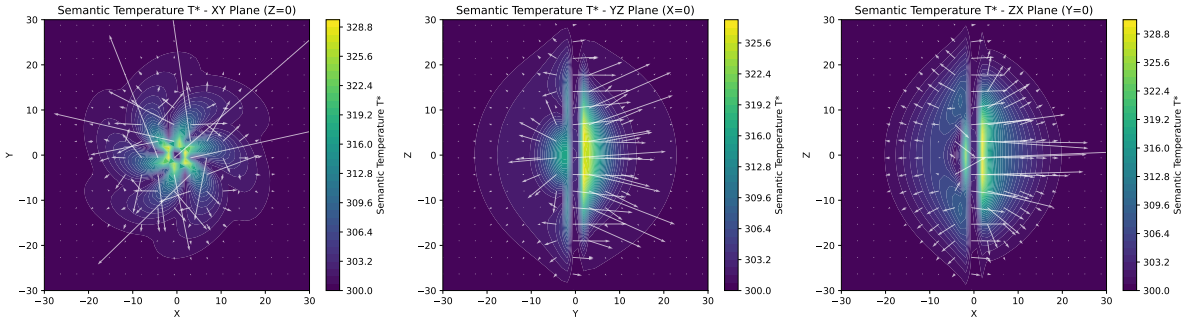

Figure 4. Semantic temperature T_* in three orthogonal planes with ($\omega = 0.1, \gamma = 0.01$). White arrows indicate semantic flux vectors. Left: XY plane ($Z = 0$) showing coronal heat structure. Center: YZ plane ($X = 0$) showing vertical flux alignment. Right: ZX plane ($Y = 0$) showing lateral flux corridors.

We propose that Hot spot events correspond to decoherence events from non-local entropy increases outside the singularity. These events may activate one, two, or all three processing channels simultaneously, depending on the spatial structure and intensity of the incoming decoherence field. A configuration exhibiting three hot spots with equilateral spacing indicates maximum processing load: all available channels are engaged in high entropy rejection. Because decoherence is intrinsically chaotic, the present model, which assumes a symmetric Gaussian impulse and uniform phase geometry, represents an idealized limit. Observed hot spot patterns are expected to deviate from this idealization, displaying one, two, or three active regions at variable angular positions within the coronal flow, consistent with the stochastic nature of entropy driven events.

In this model, the central coherence singularity operates at the fastest admissible processing rate allowed by the thermodynamic uncertainty relation. The innermost nodes of the certainty ratio field therefore correspond to maximally accelerated information-processing channels, with recursion dynamics that naturally approach relativistic limits. Hot-spot structures in the equatorial plane are not passive plasma clumps but localized coherence events propagating along these channels, so their apparent orbital motion reflects the underlying processing geometry rather than purely hydrodynamic

 doi:10.20944/preprints202601.2105.v2

circulation. This interpretation is consistent with recent analyses suggesting that GRAVITY hot spots exhibit pattern motion at super-Keplerian speeds rather than bound Keplerian orbits [19].

Together, the decoherence and temperature fields define the structure of the corona and explain the origin of its high-entropy emission. These features are structured consequences of the coherence field geometry and the thermodynamic processing rules of the system.

6. Non-Helical Geometric Structures of Jets

The certainty ratio field encodes the angular and axial structure that governs jet formation in this model. Its harmonic content produces a set of geometric features that appear consistently across the parameter range, including axial knots generated by longitudinal modulation, periodic brightening arising from angular harmonics, layered polarization produced by stacked coherence corridors, and short-lived coherent features that occur outside the black hole and resemble lensing-amplified point structures reported in high-resolution observations.

Observations of M87's jet reveal a diverse set of morphological features: discrete bright knots at the jet base with wide opening angles [20], helical threading with limb-brightened edges at intermediate scales [21], transverse kinks that produce quasi-periodic variability [22], and large-scale arc structures interpreted as signatures of jet precession [23]. The certainty ratio field naturally produces analogs of each structure through variation of a single parameter: the phase twist, which is made to represent the black holes motion through a fixed universal field as it moves through spacetime.

To illustrate these behaviors, four representative slices of the certainty ratio field are shown in Figures 5, 6, 7, and 8. Each configuration uses the same spatial domain and resolution, with the twist parameter as the only varying quantity.

1. **Zero twist (baseline coherence).** With no imposed twist ($\omega = 0$), the certainty ratio forms a symmetric axial corridor. The field exhibits vertically aligned coherence with no lateral displacement, no knot formation, and no angular bias. This configuration establishes the reference geometry for a collimated, twist-free outflow and corresponds to the wide-angle conical structures observed at the jet base [20].
2. **Small twist (microstructure regime).** A moderate twist ($\omega = 0.05$) introduces clear geometric microstructure. Localized maxima appear along the axis, producing knot-like features and periodic brightening. The angular harmonics generate a controlled helical bias while maintaining overall stability. This regime reproduces the three helical threads, limb-brightening, and spectral flattening at thread intersections observed in VLBA studies of M87 at 8 and 15 GHz [21]. The segmented brightening and polarization layering match the stacked coherence corridors predicted by the model.
3. **Looped twist (strong deformation, small scale).** At higher twist ($\omega = 0.5$), the angular phase advances rapidly across the spatial window, producing looped structures in which bright regions shift laterally and the axial corridor bends or folds. This geometry corresponds to the transverse kink deformations that disrupt the jet spine without affecting global structure [22]. The quasi-periodic radiation signatures observed in blazars arise naturally from this regime, where the certainty ratio field produces time-variable emission through localized magnetic reconnection at kink sites.
4. **Looped twist (strong deformation, large scale).** When moderate twist ($\omega = 0.1$) is applied over an extended spatial domain, the model produces large scale arc structures and lateral displacement. These features resemble the ring-like geometries observed in precessing jets [23], where time-integrated emission from a sweeping cone projects as arcs perpendicular to the jet axis. The bilateral symmetry in the YZ and ZX planes (Figure 8) predicts observable width variations depending on viewing angle, consistent with the orientation dependent jet morphologies reported in VLBI surveys.

These four figures demonstrate that the certainty ratio's angular harmonics naturally generate the full spectrum of jet microstructure: from discrete knots and helical threads at low-to-moderate

 doi:10.20944/preprints202601.2105.v2

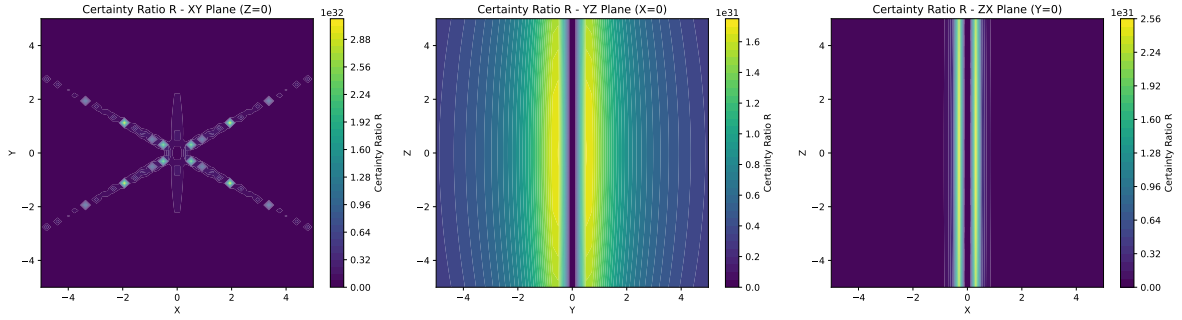

Figure 5. Certainty ratio for the zero-twist configuration ($\omega = 0, \gamma = 0$). The field exhibits a straight axial corridor with uniform vertical alignment and no angular displacement, corresponding to wide-angle conical jet structures observed at the base of M87 [20].

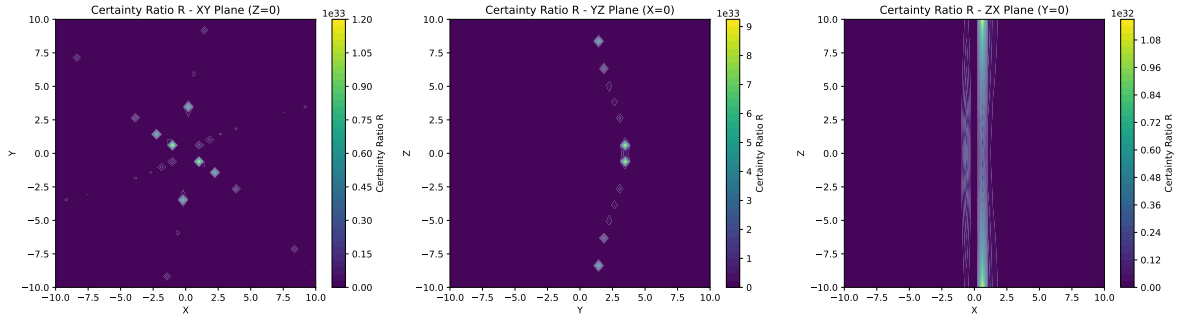

Figure 6. Certainty ratio for the small-twist configuration ($\omega = 0.05, \gamma = 0.0001$). Localized maxima form along the axis, and angular harmonics introduce a mild helical bias that produces periodic brightening. This regime matches the three helical threads and limb-brightened structure observed in M87 VLBA data [21].

twist, to transverse kinks and large-scale loops at high twist. The model does not require separate mechanisms for each morphology—all arise from the same coherence field geometry modulated by the phase twist parameter. The moderate-twist case (Figure 6) reproduces the segmented brightening, axial modulation, and polarization layering observed in M87. The high-twist cases (Figures 7 and 8) provide structural limits: small-scale kinks represent higher twist angles, while large-scale loops can occur at lower twist angles.

6.1. Coherent Exterior Emission and Geometric Image Distortion

Observations of compact objects reveal structured emission features and positional shifts that can be cataloged without committing to a specific dynamical mechanism.

In the vicinity of isolated stellar-mass objects, astrometric microlensing observations demonstrate precise, time-dependent shifts in the centroids of background light sources. These relativistic deflec-

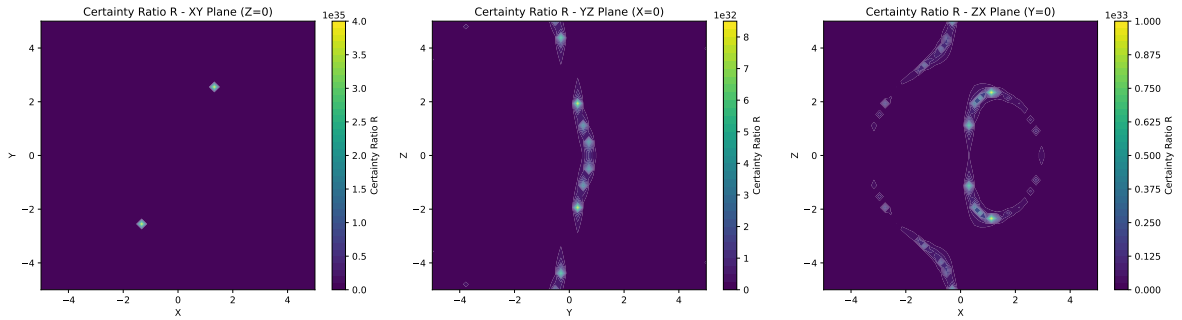

Figure 7. Certainty ratio for the looped-twist configuration ($\omega = 0.5, \gamma = 0$). Rapid angular phase advance produces small-scale looped structures and lateral displacement of bright regions, corresponding to transverse kink instabilities that generate quasi-periodic variability [22].

 doi:10.20944/preprints202601.2105.v2

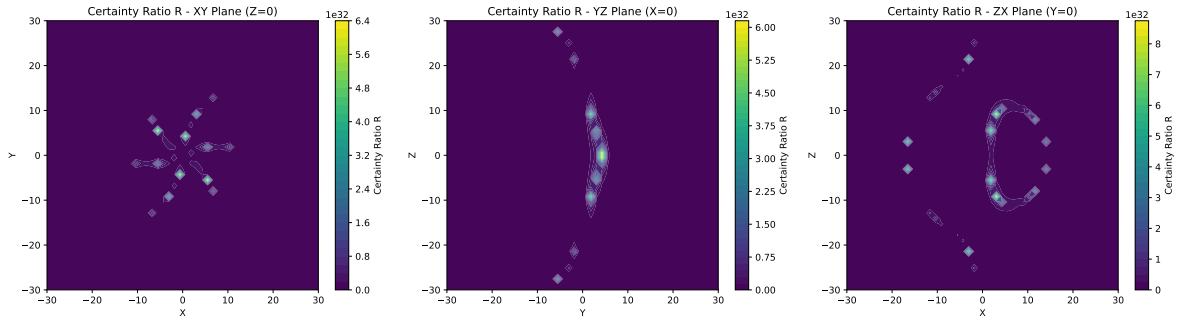

Figure 8. Certainty ratio for the large-scale looped configuration ($\omega = 0.1$, $\gamma = 0.01$). Extended spatial domain with moderate twist produces large-scale arc structures and bilateral asymmetry. This geometry resembles the ring-like features and precession-driven morphologies observed in jets with time-variable orientations [23].

tions trace specific trajectories as the background light interacts with the gravitational field, providing a direct measurement of the lens mass without requiring local luminous emission [28,29].

In larger-scale systems, such as Abell 1201, strong gravitational lensing resolves specific geometric anomalies, including tangential arcs and faint counter-images projected near the central mass. These features represent the distortion of distant light into coherent, non-local structures [30]. Furthermore, numerical renderings of background starfields in the strong-field limit show the formation of Einstein rings and multiple relativistic images that persist as stable geometric features independent of local plasma dynamics [27].

In the present theory, these transient emission features and geometric distortions that deviate from symmetry in the no-field case can be interpreted as exterior manifestations of the certainty ratio field rather than as separate phenomena. The bright, localized features and secondary images outside the black hole are identified with regions of elevated certainty ratio, where R exceeds the unity threshold and supports coherent emission channels or focused light paths.

The observed arcs, rings, and astrometric shifts correspond to longitudinal and azimuthal modulations of the same field along the vertical coherence axis, with variations in the twist parameter selecting between different lensing regimes. This mapping allows one to place observationally cataloged structures—counter-images, arcs, and rings—into a geometric reference, which is interpreted here as a direct observation of the certainty ratio field rather than purely anomalous lensed light.

7. Conclusions

This work presents a coherence and information based interpretation in which the black hole functions as a computational processor. The resulting geometry produces two orthogonal planes (equatorial and vertical), a coherent vertical outflow aligned with observed jet axes and a jet microstructure consistent with observations.

The model yields several testable observational signatures:

- The spacing and modulation of jet knots correlate to what were previously thought to be photon rings. A Jet that becomes asymmetric produces more photon ring geometry because it is processing information at increasingly obtuse angles in quasi-relativistic regimes of local black hole spacetime. Coherence and coherent light are interchangeable phenomena. The observed features are not gravitationally lensed images from behind the black hole, but rather coherent light from the black hole's computational processes comparing calculations with spacetime geometry as a result of the black hole experiencing larger and larger angular deviations in its relation to a fixed universal coherence field.
- The hot spots are non-local increases in entropy that are channeled out of the core of the black hole. A hot spot as informational decoherence is predicted to have a damping effect between the explosion an its effect on coronal acceleration and deceleration.
- The jet microstructure results from Coherence based physical processes in the core of the black hole.

 doi:10.20944/preprints202601.2105.v2

- A black hole will transition to another dimensional state after it clears its decoherence field and achieves perfect coherence. Perfect coherence is an anomaly in this dimension and represents the completion of its work.

These signatures provide a direct path for evaluating the coherence-thermodynamics against current and future observations of Sgr A*, M87*, and related systems. By linking information density to geometric phase structures, it provides a single mathematical language that connects human reasoning (semantic information) to astrophysical structures (relativistic jets).

Author Contributions: The primary author is responsible for this whole work.

Funding: This research received no external funding

Data Availability Statement: Code used for this work is available at https://colab.research.google.com/drive/1lwsyIuR6vRybMY6ZWnh8nEER1d1-zudF?usp=sharing.

Acknowledgments: Without the United States Constitution, and its emphasis on free thinking and reasoning, none of this is possible. The Author is grateful for all those who defend the USA Constitution with courage and honor. This work was inspired by and in remembrance of your sacrifices to make intellectual freedom possible.

Conflicts of Interest: The authors declare no conflicts of interest.

Abbreviations

The following abbreviations and symbols are used in this manuscript:

MDPI	Multidisciplinary Digital Publishing Institute
Sgr A	Galactic center black hole
M87	Virgo A black hole
VLBI	Very long baseline interferometry
EHT	Event Horizon Telescope
GRAVITY	VLTI near infrared interferometer
R	Certainty ratio
σ	Contradiction field
Γ	Decoherence field
T^*	Semantic temperature
F_{sem}	Semantic free energy
C-I	Coherence and Information
CCBH	Cosmologically Coupled Black Holes

References

1. Wheeler, John A. 1979. Some men make history; others reflect and write about it. In *Mysteries of the Universe*, edited by L. W. Bruvede, 24–25. Washington, DC: NASA.
2. Bekenstein, Jacob D. 1973. Black holes and entropy. *Physical Review D* 7: 2333–46. doi:10.1103/PhysRevD.7.2333.
3. Hawking, Stephen W. 1975. Particle creation by black holes. *Communications in Mathematical Physics* 43: 199–220. doi:10.1007/BF02345020.
4. Page, Don N. 1993. Average entropy of a subsystem. *Physical Review Letters* 71: 1291–94. doi:10.1103/PhysRevLett.71.1291.
5. Kocherlakota, Prashant, Luciano Rezzolla, Rittick Roy, and Maciek Wielgus. 2024. Hotspots and photon rings in spherically symmetric space–times. *Monthly Notices of the Royal Astronomical Society* 531: 3606–41. doi:10.1093/mnras/stae1321.
6. Akiyama, Kazunori, et al. (Event Horizon Telescope Collaboration). 2019. First M87 Event Horizon Telescope Results. IV. Imaging the Central Supermassive Black Hole. *The Astrophysical Journal Letters* 875: L4. doi:10.3847/2041-8213/ab0e85.
7. Chatterjee, Koushik, Matthew Liska, Alexander Tchekhovskoy, and Sera B. Markoff. 2019. Accelerating AGN jets to parsec scales using general relativistic MHD simulations. *Monthly Notices of the Royal Astronomical Society* 490: 2200–18. doi:10.1093/mnras/stz2626.

8. Yuan, Feng, and Ramesh Narayan. 2014. Hot Accretion Flows Around Black Holes. *Annual Review of Astronomy and Astrophysics* 52: 529–88. doi:10.1146/annurev-astro-082812-141003.
9. Barton, J. 2025. Coherence Thermodynamics: Structure from Contradiction. *Preprints* 2025: 2025071448. doi:10.20944/preprints202507.1448.v4.
10. Farrah, Duncan, et al. 2023. Observational Evidence for Cosmological Coupling of Black Holes and its Implications for an Astrophysical Source of Dark Energy. *The Astrophysical Journal Letters* 944: L31. doi:10.3847/2041-8213/acb704.
11. Croker, Kevin S., Zevin, Michael, Farrah, Duncan, Nishimura, Kurtis A., and Tarlé, Gregory. 2024. Cosmologically Coupled Compact Objects: A Single-Parameter Model for LIGO-Virgo Mass and Redshift Distributions. *The Astrophysical Journal Letters* 961: L31. doi:10.3847/2041-8213/ad1de1.
12. Wheeler, John A. 1983. Law without law. In *Quantum Theory and Measurement*, edited by J. A. Wheeler and W. H. Zurek, 182–213. Princeton: Princeton University Press.
13. Dirac, P. A. M. 1937. The cosmological constants. *Nature* 139: 323. doi:10.1038/139323a0.
14. Akiyama, Kazunori, et al. (Event Horizon Telescope Collaboration). 2019. First M87 Event Horizon Telescope Results. IV. Imaging the Central Supermassive Black Hole. *The Astrophysical Journal Letters* 875: L4. doi:10.3847/2041-8213/ab0e85.
15. Event Horizon Telescope Collaboration et al. 2022. First Sagittarius A* Event Horizon Telescope Results. I. The Shadow of the Supermassive Black Hole in the Center of the Milky Way. *The Astrophysical Journal Letters* 930: L12. doi:10.3847/2041-8213/ac6674.
16. Walker, R. C., et al. 2018. The Structure and Dynamics of the Subparsec Jet in M87 Based on 50 VLBA Observations over 17 Years at 43 GHz. *The Astrophysical Journal* 855: 128. doi:10.3847/1538-4357/aaafcc.
17. Kim, J., et al. 2018. 230 GHz VLBI Observations of M87: Event-Horizon-Scale Structure during an Enhanced Very-High-Energy y-Ray State in 2012. *The Astrophysical Journal* 861: 129. doi:10.3847/1538-4357/aac7c6.
18. Chan, Ho-Sang, and Chi-kwan Chan. 2025. The 230 GHz Variability of Numerical Models of Sagittarius A*. II. The Physical Origins of the Variability. *The Astrophysical Journal* 985: 164. doi:10.3847/1538-4357/adc99f.
19. Matsumoto, Tatsuya, Chan, Chi-Ho, and Piran, Tsvi. 2020. The origin of hotspots around Sgr A*: Orbital or pattern motion? *Monthly Notices of the Royal Astronomical Society* 497: 2385–2392. doi:10.1093/mnras/staa2095.
20. Miyoshi, Makoto and Kato, Yoshiaki and Makino, Junichiro. 2022. The Jet and Resolved Features of the Central Supermassive Black Hole of M87 Observed with the Event Horizon Telescope (EHT). *The Astrophysical Journal* 933: 36. doi:10.3847/1538-4357/ac6ddb.
21. Nikonov, A. S., Kovalev, Y. Y., Kravchenko, E. V., Pashchenko, I. N., and Lobanov, A. P. 2023. Properties of the jet in M87 revealed by its helical structure imaged with the VLBA at 8 and 15 GHz. *Monthly Notices of the Royal Astronomical Society* 526: 5949–5963. doi:10.1093/mnras/stad3061.
22. Dong, Lingyi, Zhang, Haocheng, and Giannios, Dimitrios. 2020. Kink Instabilities in Relativistic Jets Can Drive Quasi-Periodic Radiation Signatures. *Monthly Notices of the Royal Astronomical Society* 494: 1817–1825. doi:10.1093/mnras/staa773.
23. Britzen, S., et al. 2021. A Ring Accelerator? Unusual Jet Dynamics in the IceCube Candidate PKS 1502+106. *Monthly Notices of the Royal Astronomical Society* 503: 3145–3178. doi:10.1093/mnras/stab589.
24. Walker, R. C., Hardee, P. E., Davies, F. B., Ly, C., and Junor, W. 2018. The Structure and Dynamics of the Subparsec Jet in M87 Based on 50 VLBA Observations over 17 Years at 43 GHz. *The Astrophysical Journal* 855: 128. doi:10.3847/1538-4357/aaafcc.
25. Nikonov, A. S., Kovalev, Y. Y., Kravchenko, E. V., Pashchenko, I. N., and Lobanov, A. P. 2023. Properties of the jet in M87 revealed by its helical structure imaged with the VLBA at 8 and 15 GHz. *Monthly Notices of the Royal Astronomical Society* 526: 5949–5963. doi:10.1093/mnras/stad3061.
26. Yuan, Feng, and Narayan, Ramesh. 2014. Hot Accretion Flows Around Black Holes. *Annual Review of Astronomy and Astrophysics* 52: 529–588. doi:10.1146/annurev-astro-082812-141003.
27. James, O., von Tunzelmann, E., Franklin, P., and Thorne, K. S. 2015. Gravitational Lensing by Spinning Black Holes in Astrophysics, and in the Movie Interstellar. *Classical and Quantum Gravity* 32: 065001. doi:10.1088/0264-9381/32/6/065001.
28. Lam, C. Y., et al. 2022. An isolated mass gap black hole or neutron star detected with astrometric microlensing. *The Astrophysical Journal Letters* 933: L23. doi:10.3847/2041-8213/ac7442.
29. Sahu, K. C., et al. 2022. An Isolated Stellar-mass Black Hole Detected through Astrometric Microlensing. *The Astrophysical Journal* 933: 83. doi:10.3847/1538-4357/ac739e.
30. Smith, R. J., et al. 2023. Abell 1201: detection of an ultramassive black hole in a strong gravitational lens. *Monthly Notices of the Royal Astronomical Society* 521: 3298–3312. doi:10.1093/mnras/stad027.

 doi:10.20944/preprints202601.2105.v2